Green, nonchemical route for the synthesis of MnWO$_4$ nanostructures, evaluation of their photocatalytic and electrochemical performance

G. S. Shivaganga[1], P. Parameswara[1,*], C. Mallikarjunaswamy[2,*] , K. C. Sunil Kumar[3],
T. L. Soundarya[4], G. Nagaraju[5], S. Punith[6], and V. Lakshmi Ranganatha[7]

[1] *Department of Physics, The National Institute of Engineering, Manandavadi Road, Mysuru, Karnataka 570008, India*
[2] *Postgraduate Department of Chemistry, JSS College of Arts,*
Commerce and Science and JSS Research Centre (A Recognized Research Centre of University of Mysore), Mysuru, Karnataka 570025, India
[3] *Postgraduate Department of Physics, JSS College of Arts,*
Commerce and Science and JSS Research Centre (A Recognized Research Centre of University of Mysore), Mysuru, Karnataka 570025, India
[4] *Department of Studies and Research in Chemistry, University College of Science, Tumkur University, Tumakuru, Karnataka 572 103, India*
[5] *Energy Materials Research Laboratory, Department of Chemistry, Siddaganga Institute of Technology, Tumakuru, Karnataka 572103, India*
[6] *Department of Chemistry, Indian Institute of Technology (IIT), Hyderabad, Sangareddy, Telangana 502 285, India*
[7] *Department of Chemistry, The National Institute of Engineering, Manandavadi Road, Mysuru, Karnataka 570008, India*

ABSTRACT

This research article presents the synthesis of MnWO$_4$ nanoparticles using a combination of MnCl$_2$ and Na$_2$WO$_4$·2H$_2$O as precursors, with water as the sole solvent for dissolution, eliminating the need for additional solvents. The synthesized materials underwent comprehensive characterization employing various analytical techniques, including X-ray diffraction, scanning electron microscopy, UV–visible spectrophotometry, and Fourier Transform Infrared Spectrometry. The photocatalytic activity of MnWO$_4$ nanoparticles for degrading the organic contaminant methylene blue in water was also investigated under visible light irradiation. Notably, a significant degradation of methylene blue was observed, with 98% degradation achieved within a 120-min irradiation period. Additionally, the material was subjected to electrochemical studies to assess its sensing capabilities and exhibited strong sensing activity by detecting nano-molar concentrations of nitrite solution.

Address correspondence to E-mail: paramphysics@nie.ac.in; mallik.aanekere@gmail.com

Springer

1 Introduction

Against the backdrop of the rapid advancements in energy crisis and environmental pollution, researchers face a significant challenge. Harnessing the full potential of solar energy through photocatalysts to efficiently split water into oxygen and hydrogen remains a formidable task. In recent years, untreated textile industrial effluents containing complex colored substances have posed both aesthetic and environmental issues by contaminating water bodies. Traditional water treatment techniques, including activated charcoal adsorption, flocculation, and biological treatment, have proven ineffective in addressing this problem. Consequently, researchers have turned to the method of photocatalysis as an effective solution. In comparison to conventional methods, catalytic degradation of effluents offers several advantages, including minimal waste disposal, absence of pressure or temperature requirements, and the utilization of environmentally available oxygen as an oxidant. Given these numerous benefits, photocatalytic degradation emerges as a promising approach for effluent treatment. Nanotechnology and material science play vital roles in synthesizing inorganic photocatalyst structures with nanoscale dimensions and diverse morphologies [1–9]. Many inorganic materials [10] like ZnO [11], $BiVO_4$ [12], $Mn_2V_2O_7$ [7], BiOI [13, 14], BiOCl [15], CdO [11, 16], CuO [17], NiO [18], $Bi_{14}W_2O_{27}$ [19], TiO_2 [20] CeO_2 [21] have been synthesized in the last decade using methods such as microwave [22], hydrothermal [23], and precipitation. Metal oxide nanomaterials have garnered significant research attention in recent years, thanks to their exceptional properties and ultrafine structures. Among the various metal oxides, transition metal tungstates of the form MWO_4 (where M represents Fe, Co, Ni, Cu, Zn, and Cd) have found wide-ranging applications in interdisciplinary fields due to their unique physicochemical properties at the nanoscale [24]. One such tungstate, $MnWO_4$, exhibiting the wolframite phase, has captured extensive research interest due to its potential applications in molecular imaging [25], photocatalysis [26], multiferroic materials [25], electrochemical devices [27], and humidity sensors [9]. Furthermore, $MnWO_4$ demonstrates important electrochromic properties, coupled with long-term structural stability [28].

Among these, $MnWO_4$ is a complex compound with interesting physical and chemical properties and is extensively used as a high-sensitive sensor in many industries, such as medicine, meteorology, agriculture, domestic and food [27, 29–41]. In addition to these properties, $MnWO_4$ also has attractive magnetic properties [30, 42].

Conventional methods of synthesizing $MnWO_4$ nanomaterials typically involve high-temperature treatment at 1000 °C and grinding, resulting in heterogeneous and non-uniform nanostructures. In contrast, the adoption of green synthesis, which employs eco-friendly and cost-effective non-hazardous chemicals, has gained popularity due to its numerous advantages. Green synthesis utilizes reducing agents such as bacteria, fungi, and plants, with phytochemicals from plants playing a pivotal role in reducing chemical usage and enhancing the production of safe products [43]. Moreover, phytochemicals possess the ability to modulate the shape and size of inorganic compounds due to their surface activity. In this research article, we present the surfactant- and fuel-free synthesis of $MnWO_4$ nanoparticles, successfully yielding pebble-shaped nanomaterials with a substantial surface area, which exhibited excellent catalytic activity. Additionally, we evaluated the modified glassy carbon electrodes for the electrochemical detection of nitrites [44, 45].

2 Experimental procedure

2.1 Materials used

All chemicals used were of analytical grade. Manganese chloride ($MnCl_2 \cdot 4H_2O$, 99%), sodium tungstate ($Na_2WO_4 \cdot 2H_2O$) and MB dye were purchased from SD Fine chemicals limited Company, Mumbai, India, and used without further purification. Sodium nitrite was purchased from Sigma Aldrich Company.

2.2 Synthesis of $MnWO_4$ nanoparticles

To prepare $MnWO_4$ nanoparticles, sources of 0.1 M manganese chloride and 0.1 M sodium tungstate dihydrate were dissolved in a small amount of water and added to a crucible. The mixture was stirred for about 15 min on a hot plate to obtain a homogeneous semi-solid liquid. The crucible was then placed in a 500 °C pre-heated muffle furnace, where a smoldering-type reaction took place with the liberation of gases within 15 min. The resulting product was subjected to calcination for 4 h at 500 °C to remove all impurities, as
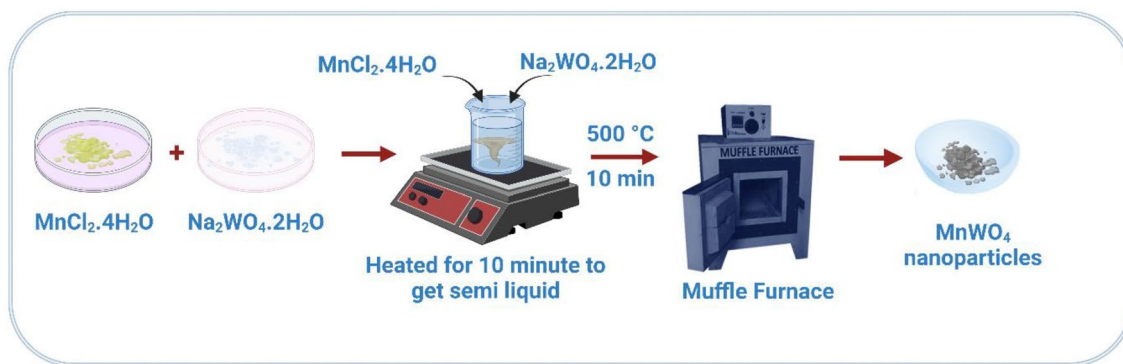
Scheme 1 Schematic representation of synthesis of MnWO$_4$ nanoparticles

shown in Scheme 1. The synthesized nanomaterials were used for electrochemical applications and to study the photodegradation of the methylene blue organic dye.

2.3 Characterization techniques

The crystal structure and phase purity of the synthesized nanoparticles were confirmed using various instruments. X-ray diffraction analysis was performed using a Rigaku smart lab X-ray diffractometer with Cu-Kα (1.5418) radiation at a scanning rate of 1θ/min. Functional groups were identified between the wave number ranges of 400 to 4000 cm^{-1} using an Agilent spectrophotometer (FT-IR). The UV–Visible absorption spectrum of MnWO$_4$ Nps was examined using a Cary-60 Agilent Technologies spectrophotometer. Optical properties in the wavelength range of 200–500 nm (DRS) were measured using a SHIMADZU spectrophotometer make UV-26001. The purity of the sample and the surface morphology of the nanoparticles were examined using a TESCAN Vega 3LMU scanning electron microscope (SEM) with electron-dispersive X-ray. Raman measurements were taken using a Horiba Xplora Plus Raman microscope. The shape and size of the nanoparticles were observed using a JEOL 2100 transmission electron microscope (TEM). The sensitivity was checked using an Electrochemical Workstation: CH instrument (CH1655E) instrument.

2.4 Photocatalytic activity

The photocatalytic activity of MnWO$_4$ in degrading methylene blue dye in water under visible light irradiation was investigated. The degradation efficiency was determined using a HEBER scientific photo-reactor, which contained a water-circulating jacket to trap visible light (400 W, Tungsten Lamp) and fans to eliminate heat generated by the light source. 50 mg of photocatalyst was added to a 9-inch long quartz tube containing 5 ppm (100 mL) of methylene blue. The mixture was left in the dark for 30 min to reach adsorption–desorption equilibrium. Every 20 min, the mixture was removed from the reactor, centrifuged to separate the photocatalyst from the solution, and the absorption was measured using a UV–visible spectrophotometer to determine the percentage of degradation. The degradation efficiency also depends on factors such as the catalyst load, the pH of the solution, and the concentration of dye. All these parameters were examined and optimized to achieve the best degradation efficiency.
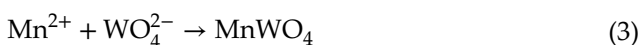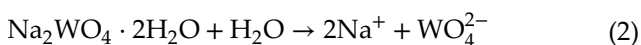
2.5 Procedure for the modification of electrode and electrochemical studies

Preconditioning of the glassy carbon electrode (GCE) is crucial in studying its electrochemical properties. The GCE was first rubbed in a circular motion using various particle sizes of aluminum oxide (Al$_2$O$_3$) at 1.0, 3.0, and 0.05 μm. The electrode was then immersed in deionized water and sonicated for 10 min to remove any traces of Al$_2$O$_3$ adsorbed on its glassy surface. The polished surface was coated with MnWO$_4$ nanoparticles (1 mg/mL) and left to dry for 30 min. The modified GCE was used to assess its electrochemical properties using cyclic voltammetry (CV) with a C–H instrument (CH1655e) [46–48]. An electrochemical cell was set up with a volume of 10 mL in the electrode container, using the modified GCE as the working electrode, a

platinum electrode as the counter electrode, and an Ag–AgCl electrode as the reference electrode. Cyclic voltammograms were plotted for the bare GCE, the modified electrode with and without nitrite solution. The nitrite solution was used as the analyte and the buffer solution had a pH of 12.

3 Results and discussion

In this study, a one-step and quick thermal decomposition method was employed to synthesize visible active $MnWO_4$ nanoparticles. The precursors play an important role in shaping and reducing the size of the $MnWO_4$ nanoparticles. Varying molar solutions of the precursors were created using 0.01 M, 0.05 M, 0.1 M, and 0.15 M of the precursors (Mole ratio of $MnCl_2$ and $Na_2WO_4 \cdot 2H_2O$ was 1:1). The 0.1 M solution resulted in good shaping and smaller size compared to the other mole ratios. The formation mechanism of the $MnWO_4$ nanoparticles is as follows:

$$MnCl_2 + H_2O \rightarrow 2Cl^- + Mn^{2+} \tag{1}$$

$$Na_2WO_4 \cdot 2H_2O + H_2O \rightarrow 2Na^+ + WO_4^{2-} \tag{2}$$

$$Mn^{2+} + WO_4^{2-} \rightarrow MnWO_4 \tag{3}$$

3.1 Material characterization

The X-ray diffraction pattern, depicted in Fig. 1. It shows the well-defined and sharp peaks that indicates the single phase formation of $MnWO_4$ without any impure phases. The observed diffraction peaks at $2\theta = 15.38°$, $18.35°$, $23.53°$, $24.03°$, $29.78°$, $30.24°$, $31.05°$, $36.0°$, $37.21°$, $40.2°$, $48.21°$, $49.20°$, $51.18°$, $52.0°$, $60.59°$ and $64.51°$ corresponding to the planes of (0 1 0), (1 0 0), (0 1 1), (1 1 0), (− 1 1 1), (1 1 1), (0 2 0), (1 2 0), (2 0 0), (1 0 2), (0 2 2), (2 2 0), (1 3 0), (0 3 2), (2 0 2) and (1 4 0) respectively. The calculated structural parameters, $a = 4.829$ Å, $b = 5.759$ Å, $c = 4.998$ Å and $\beta = 91.16°$ discloses the monoclinic structure of $MnWO_4$. The space group of $MnWO_4$ is P2/c and the point group is C2h with two formula units per primitive cell. All peaks match well with JCPDS No. 13-434 structure, and the absence of additional peaks in the spectrum confirms the purity of the material. The mean crystalline size was estimated using Debye–Scherrer's equation:
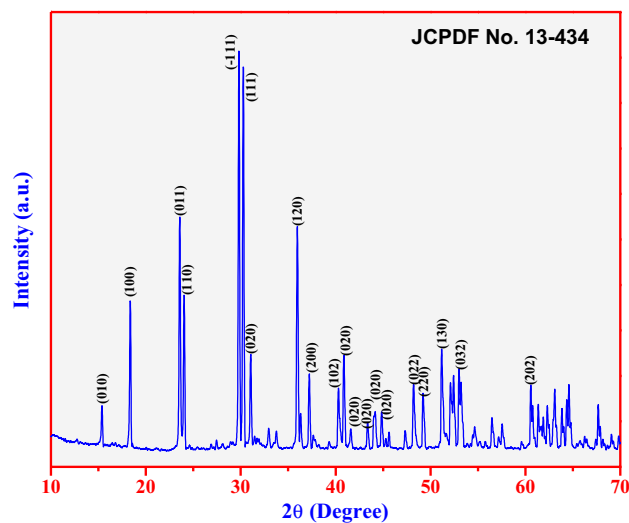

Fig. 1 X-ray diffraction pattern of $MnWO_4$ nanoparticles

$$D = \frac{0.89\lambda}{\beta \cos \theta}$$

where D is the crystallite size, λ is the X-ray wavelength, β is the full width at the half maximum, and θ is the diffraction angle. The crystallite size was found to be 61 nm.

The Raman spectroscopy was employed to elucidate the structural properties of $MnWO_4$ nanoparticles. We used the technique to investigate the lattice parameters. The Raman modes of vibrations showed strong polarization, with some modes being weak or forbidden (as seen in Fig. 2). The Table 1 lists the wavenumbers that correspond to the Raman active modes and their symmetric modes. The bands at 91.1, 127.7, and 165.5 cm^{-1} correspond to the translational mode of tungsten. The peak at 541 cm^{-1} is attributed to the stretching vibration of Mn–O bonds, while the peak at 399 cm^{-1} corresponds to the W–O–W symmetric stretching vibration. A weak band appearing at 257 cm^{-1} is due to the twisting mode of WO_2. The modes at 886.7 cm^{-1} and 774.5 cm^{-1} are assigned to the symmetric and asymmetric stretching of the W–O bond, respectively [29, 42]. In Raman spectroscopy A (Mullikan Symbol) singly degenerate or one dimensional) symmetric with respect to rotation of the principle axis. B (Mullikan Symbol) singly degenerate or one dimensional) anti-symmetric with respect to rotation of the principle axis. Subscript g symmetric with respect to the inversion center and subscript u anti-symmetric with respect to the inversion center. A group theory table is available for all point groups,
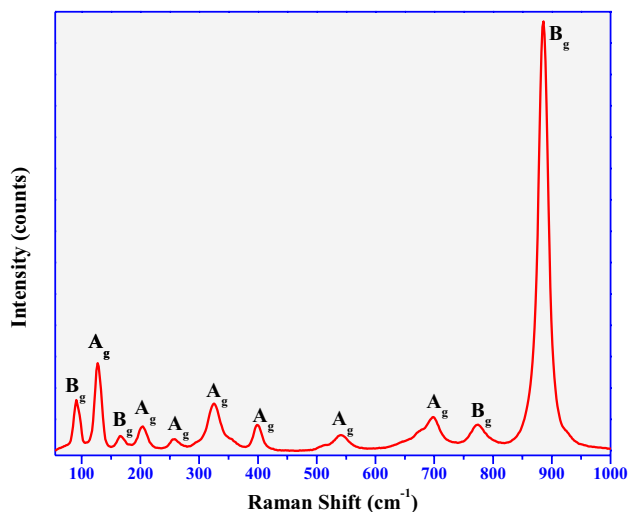
Fig. 2 Raman spectrum of MnWO$_4$ nanoparticles with scattering geometries

Table 1 Raman modes of with MnWO$_4$ nanoparticles symmetric modes

Wavenumber (cm^{-1})	Symmetry mode
91.1	Bg
127.7	Ag
165.5	Bg
202.9	Ag
256.8	Ag
324.9	Ag
398.6	Ag
541.1	Ag
697.3	Ag
773.4	Bg
885.5	Ag

which outlines the symmetry behavior of each vibration within a molecule belonging to that specific point group. Four letters, namely A, B, E, and T, are used to assign vibrations to their corresponding irreducible representation in a given point group. A and B signify singly degenerate vibrations, while E represents doubly degenerate vibrations, and T signifies triply degenerate vibrations.

The surface morphological features of MnWO$_4$ nanoparticles were evaluated through scanning electron microscope (SEM) and transmission electron microscope (TEM) analysis, which are shown in Figs. 3 and 4, respectively. The selected area electron diffraction (SAED) pattern infers the crystalline nature of the

MnWO$_4$, as only spots were observed in the image, with no rings present. The HRTEM image in Fig. 4a–d reveals lattice spacings of 0.57 nm, corresponding to the interplanar distances of the (100) crystalline plane of monoclinic MnWO$_4$ nanoparticles. These values are in excellent agreement with the results obtained from PXRD. Figure 4d displays the recorded Selected Area Electron Diffraction (SAED) patterns of a single particle. The bright spots observed in the SAED pattern were indexed to the crystalline planes (121), (202), and (212), based on the distance between the spots and the transmitted spot. The energy dispersive spectrum shows the presence of Mn, W, and O, with the percentage ratios by atoms being 17.9, 11.84, and 70.26, respectively (Fig. 5).

The Fourier transform infrared spectrum of synthesized MnWO$_4$ nanoparticles recorded in the range 400–4000 cm^{-1} is shown in Fig. 6. The sharp, peaks at 415 cm^{-1}, 449 cm^{-1}, and 486 cm^{-1}, is due to symmetric and bending vibrations of Mn–O bonds. At 570 cm^{-1}, peaks that represents stretching and bending vibrations of the W–O bond, and at 803 cm^{-1} the peak indicates symmetric stretching vibration of W–O–W bonds.

The properties of nanomaterials are greatly influenced by their surface properties, which include parameters such as surface area, pore size, and pore volume. The N$_2$ adsorption/desorption isotherm and pore size distribution of MnWO$_4$ nanoparticles reveal a type IV isotherm with Langmuir hysteresis, indicating the presence of specific-shaped pores in the sample, as depicted in Figs. 7 and 8. The surface area of the MnWO$_4$ nanoparticles was determined to be 26.9 m^2/g.

Band gap measurement, the purpose of this study was to determine the optical band gap energy (E_g) of MnWO$_4$ nanoparticles by analyzing their UV–Visible diffuse reflectance spectrum. The estimation of E_g involved using the Kubelka and Munk method. A plot was created with $(\alpha h\gamma)^2$ on the y-axis and photon energy ($h\gamma$) on the x-axis. The tangent to the linear section of the plot was extended to the x-axis, allowing the intercept to be obtained. This intercept represented the E_g value of the sample [49]. By referring to Fig. 6, it can be observed that the E_g value of MnWO$_4$ was measured to be 2.65 eV. This value aligns with previous reports on the optical band gap energy of manganese tungstate [50]. The band gap of MnWO$_4$ nanoparticles is 2.65 eV, which is remarkably low. This low band gap determines the material's excellent conductivity, making it highly efficient and suitable for the degradation of MB under
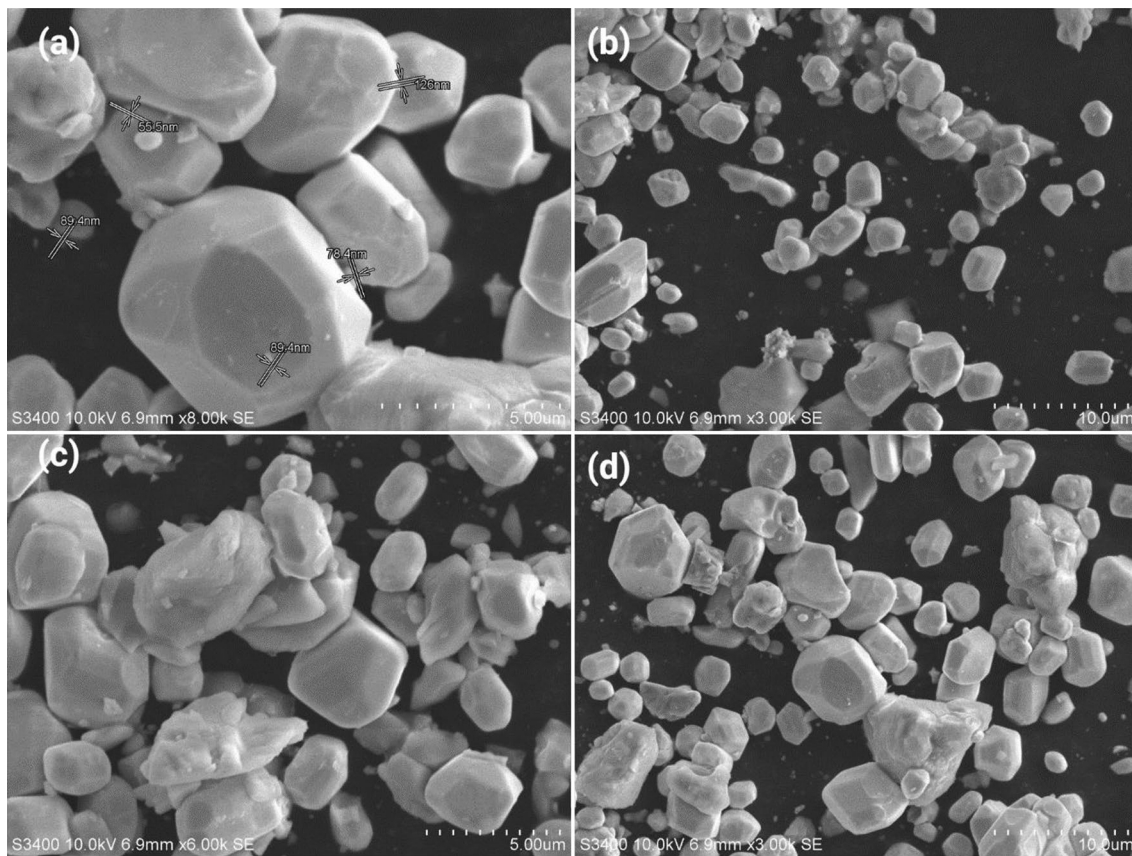
Fig. 3 SEM images as-prepared MnWO$_4$ nanoparticles

visible light irradiation alone. Many attempts have been made to reduce the band gap of materials with high band gaps through mechanisms such as doping and combining them with other materials that have lower band gaps. However, MnWO$_4$ possesses a naturally low band gap, which is a positive characteristic of this substance. Furthermore, this low band gap creates a shorter path and facilitates electron transfer, as the primary degradation mechanism involves the movement of electrons from the valence band to the conduction band. These electrons are crucial for the photoreduction process, which leads to further degradation of the dye. Moreover, these electrons also play a significant role in the catalytic behavior of electrochemical nitrite sensing. The smaller band gap of MnWO$_4$ enables enhanced MB degradation and efficient nitrite detection (Fig. 9).

4 Photocatalytic activity of MnWO$_4$ nanomaterials

In this study, the degradation of methylene blue dye in water using visible light irradiation and MnWO$_4$ as a photocatalyst was investigated. To determine the degradation efficiency, the HEBER scientific photoreactor was used, which included a water circulating jacket and fans to eliminate heat generated by the light source. To reach adsorption–desorption equilibrium, 50 mg of photocatalyst was added to a quartz tube containing 5 ppm of 100 mL of methylene blue and left in the dark for 20 min. The solution was then exposed to a tungsten lamp (400W) fitted inside a quartz chamber surrounded by a water-cooled condenser. The mixture was removed from the reactor at
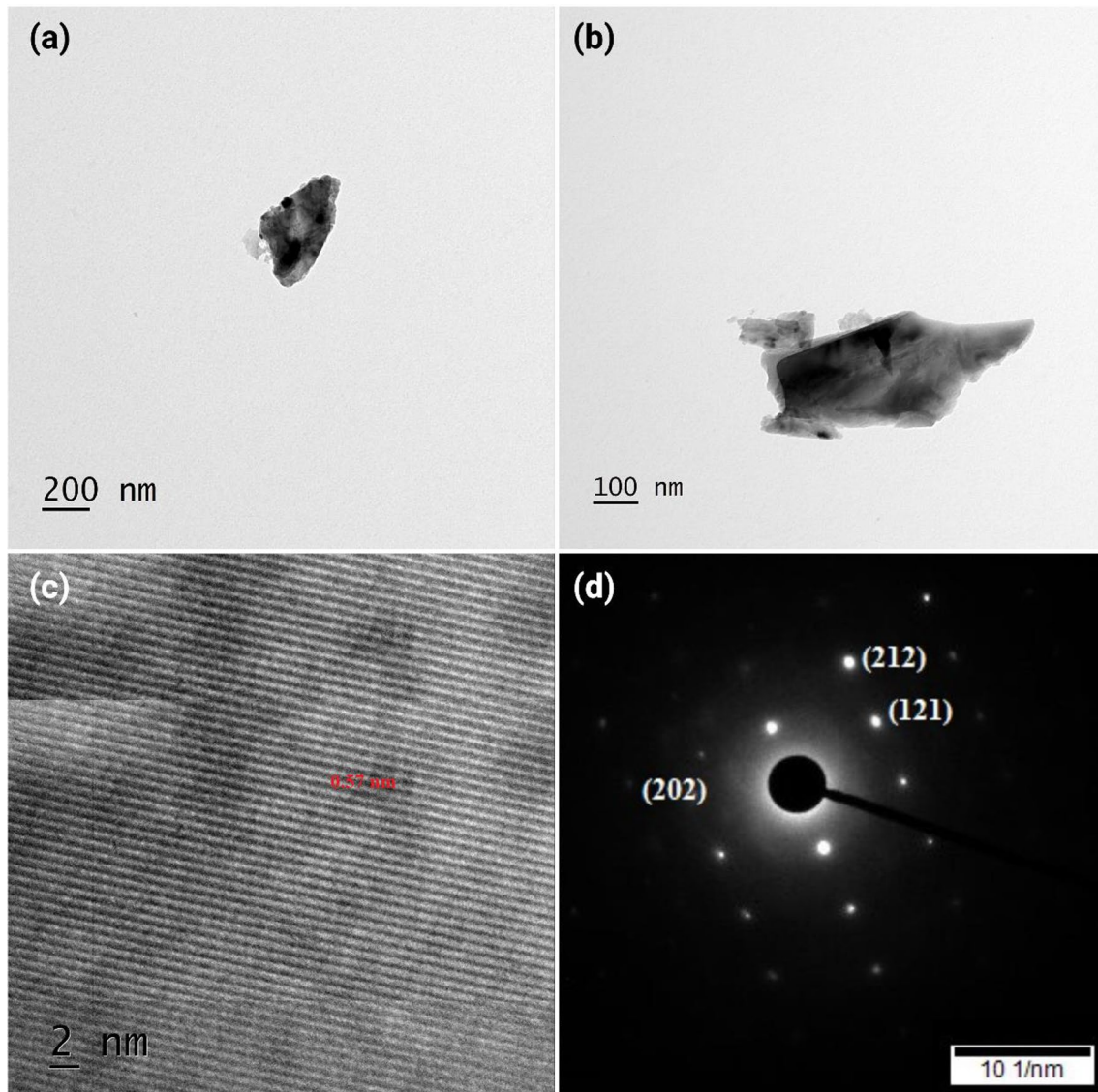
Fig. 4 TEM images (**a**, **b** and **c**) and SAED pattern (**d**) of as-prepared $MnWO_4$ nanoparticles

20-min intervals and centrifuged to separate the photocatalyst from the solution. The degradation efficiency was measured using a UV–visible spectrophotometer to determine the percentage of degradation after each interval. The optimization of degradation efficiency involved examining various parameters, such as catalyst load, pH of the solution, and dye concentration.

4.1 Effect of photocatalyst dosage

Figure 10 depicts the results of an investigation into several different doses of $MnWO_4$ nanoparticles, including doses of 10 mg, 20 mg, 30 mg, and 40 mg. The highest removal efficiency, which was found to be 99%, occurred at the 30 mg dose. However, increasing the dose to 40 mg led to a slight decrease in efficiency to 60%. This decrease was due to the strong light absorption of the $MnWO_4$ nanoparticles, which caused

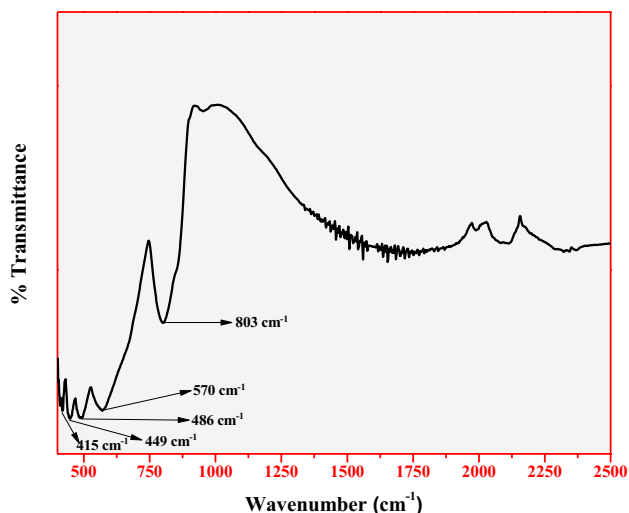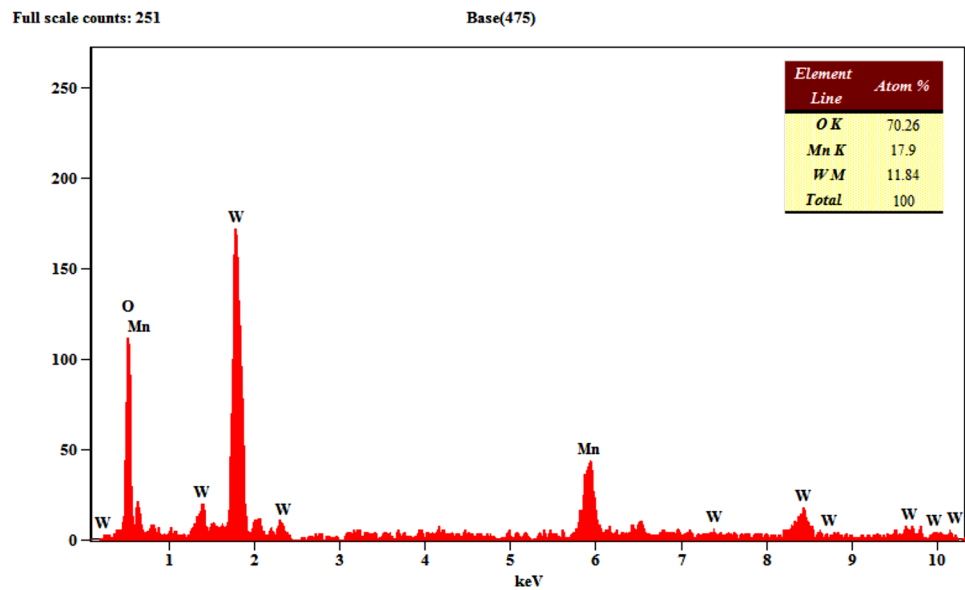**Fig. 5** EDS spectrum as-prepared $MnWO_4$ nanoparticles

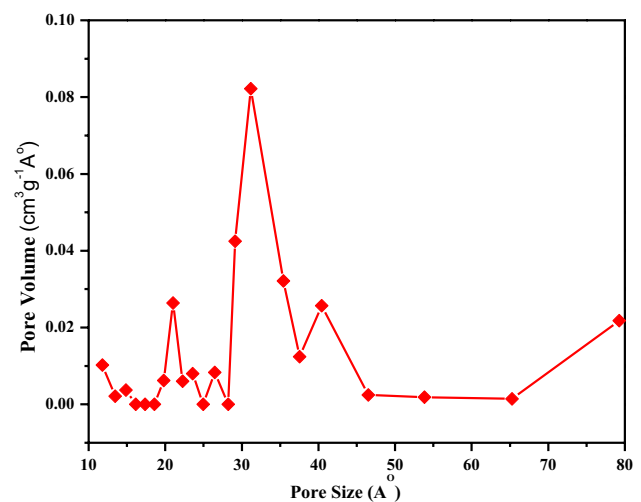**Fig. 6** FTIR spectrum of as-prepared $MnWO_4$ nanoparticles

Fig. 7 N_2 adsorption–desorption isotherm of $MnWO_4$ nanoparticles

an increase in the generation of photogenerated electrons and holes. These charge carriers then reacted with dissolved oxygen and water, producing superoxide and hydroxyl radicals. As the dose increased, light transmittance decreased, leading to reduced utilization of light and a decrease in photodegradation efficiency. Further increases in the dose caused the nanomaterials to aggregate, resulting in a further reduction in efficiency.

By keeping 30 mg of $MnWO_4$ nanoparticles constant, Fig. 11 demonstrates the optimization of dye concentration for better photocatalytic degradation

of methylene blue, with concentrations ranging from 5 to 20 ppm. The figure shows a gradual decrease in photodegradation efficiency from 99 to 60%, with the most effective degradation rate occurring at 5 ppm. The analysis suggests that the increased number of dye molecules adsorbing onto the catalyst's surface results in decreased dye degradation. Additionally, the increase in dye concentration and the decrease in light penetration may also be contributing factors to the decrease in methylene blue degradation.

In Fig. 12, a series of reaction experiments were conducted with constant dye concentration and varying
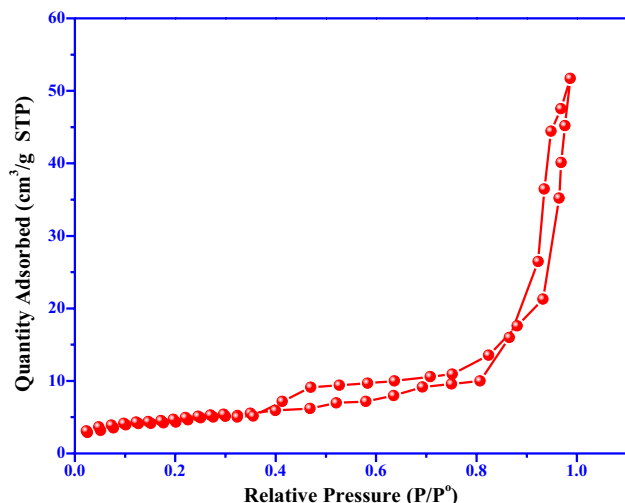
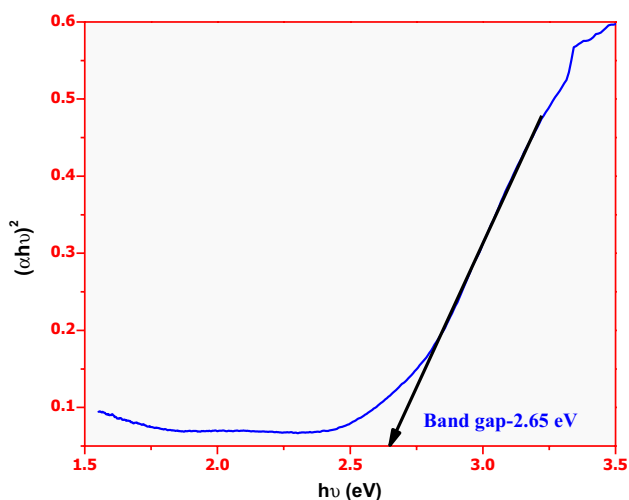**Fig. 8** Pore size distribution of MnWO$_4$ nanoparticles

Fig. 10 Photodegradation of 5 ppm MB dye with different photocatalyst dosages of MnWO$_4$ nanoparticles at pH 11

Fig. 9 Tauc plot of MnWO$_4$ nanoparticles

Fig. 11 Photodegradation of MnWO$_4$ nanoparticles as a function of irradiation time at different concentrations of methylene blue dye

catalysts at different pH ranges (3–11). The optimization of pH for dye photodegradation revealed that in an alkaline medium, there was greater degradation of MB. Specifically, at pH 11, the highest rate of dye degradation was observed, as explained by the concept of zero point charge (ZPC). The presence of adsorbed OH⁻ ions caused the surface to become negatively charged, facilitating the formation of OH· radicals, which acted as the primary oxidizing species responsible for dye degradation. Figure 12 clearly demonstrates that the pH value of the dye solution significantly influences the photodegradation of MnWO$_4$.
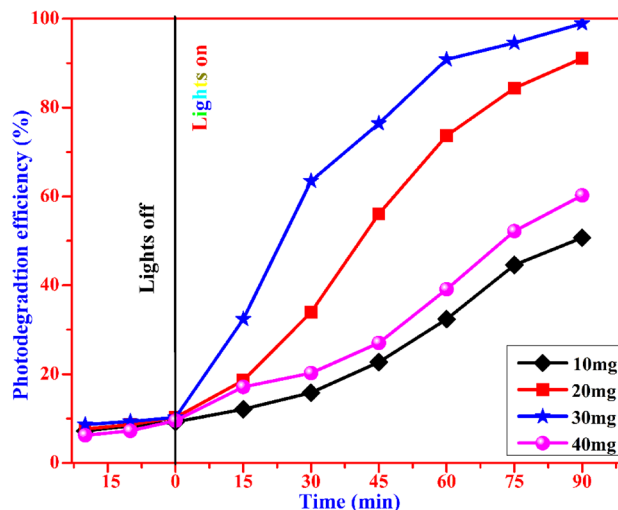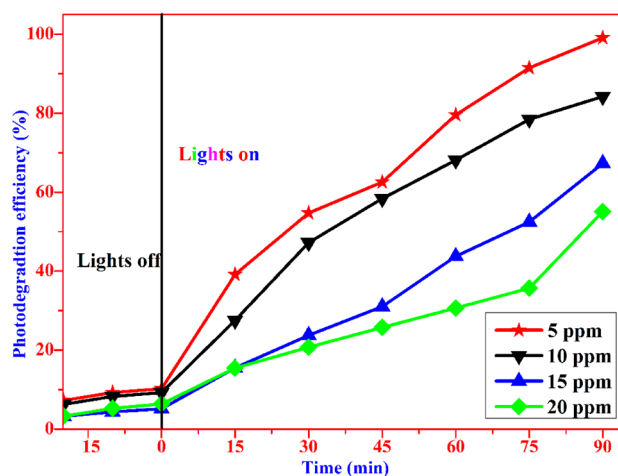
Above pH 11, the MB dye is no longer protonated, resulting in the adsorbate ceasing to absorb the dye. This is due to the electrostatic repulsion between the surface charges on the adsorbent. Consequently, the rate of MB dye degradation decreased beyond pH 11.

Degradation reactions exhibit pseudo-first-order kinetics, they are second-order bimolecular reactions that perform similar to first-order reactions as the quantity of water in the reaction is too high. A further demonstration that this reaction is a pseudo-first order reaction is provided by the graph of ln (C_o/C_t) vs. time of the reaction, where C_o and C_t are the concentrations of the dye at time '0' min and 't'
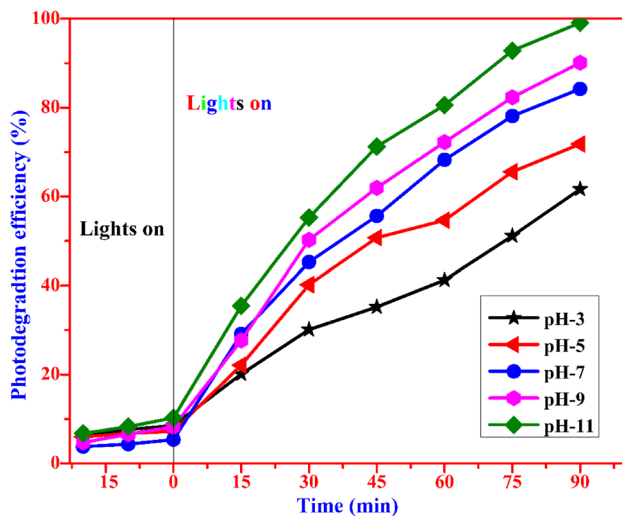
Fig. 12 Photodegradation of $MnWO_4$ nanoparticles as a function of irradiation time at different pH values

Table 2 Rate constants for the methylene blue degradation

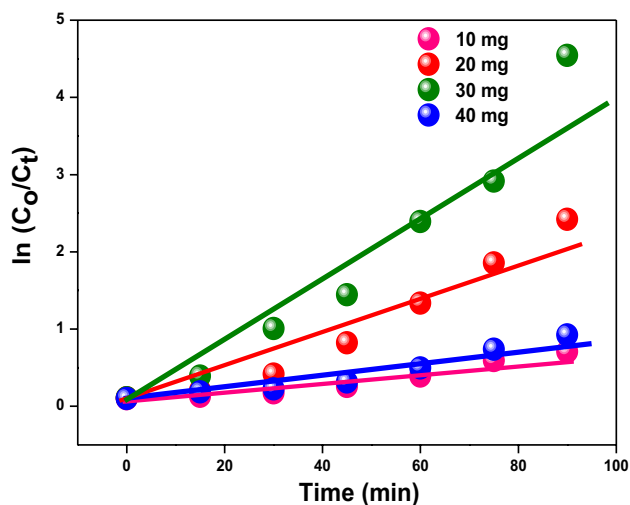| Catalyst amount (mg)	Rate constant (k), (min^{-1})
10	7×10^{-3}
20	25.8×10^{-3}
30	48.6×10^{-3}
40	9.0×10^{-3}

Fig. 13 Degradation kinetics of MB dye for catalyst variation studies

min, respectively. It shows a straight line with a positive slope and degradation rate is varying with the inverse of the concentrations of the dye at time 't'. Table 2 contains the calculated and listed rate constants for the MB degradation using 10, 20, 30, and 40 mg of catalyst.

These rate constants, with the maximum rate constant of 48.6×10^{-3} min^{-1}, indicate that the rate of the degrading reaction is found to be substantially faster at 30 mg of catalyst. Therefore, the optimal photocatalyst dosage for the highest level of MB degradation is 30 mg (Fig. 13).

4.2 Photocatalytic activity mechanism

Heterostructures demonstrate superior photocatalytic activity and possess a greater ability to separate electrons and holes compared to pure semiconductors. When $MnWO_4$ nanoparticles are irradiated with visible light, photogenerated electrons and holes are generated and contribute to redox reactions that oxidize water and reduce oxygen, resulting in the formation of highly reactive oxygen species, such as peroxides, superoxide, and hydroxyl radicals. These photogenerated reactive oxygen species are responsible for the oxidative degradation of methylene blue organic dye into mineralization products, including carbon dioxide and water, as shown in Fig. 14.

4.3 Photo stability

The success of the photocatalytic system is heavily reliant on the photocatalyst's ability to be regenerated without negatively impacting its photodegradation efficacy. To test the photocatalyst's recyclability, 50 mg of $MnWO_4$ nanoparticles were exposed to visible light (400W, Tungsten Lamp). After each cycle, the catalyst was washed multiple times with distilled water and then dried in an oven at 110 °C for 2 h. As demonstrated in Fig. 15, the regenerated catalyst displayed almost identical efficiency to the newly used catalyst for up to five cycles. However, there was a slight 3% decrease in efficiency after the sixth cycle. Nonetheless, the $MnWO_4$ nanoparticles demonstrate good stability and recyclability throughout the photochemical reaction.

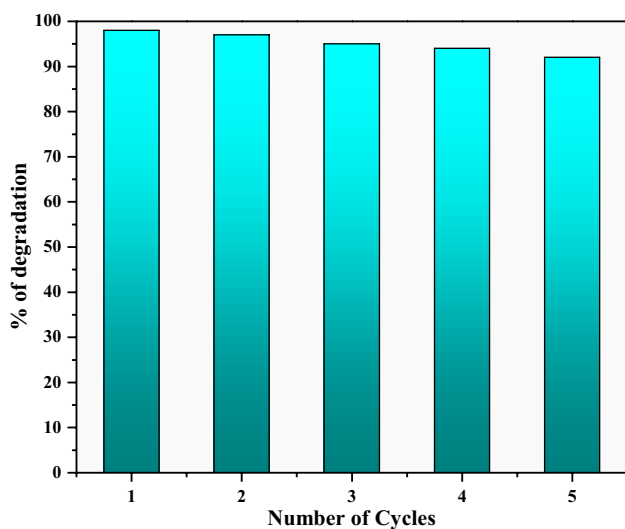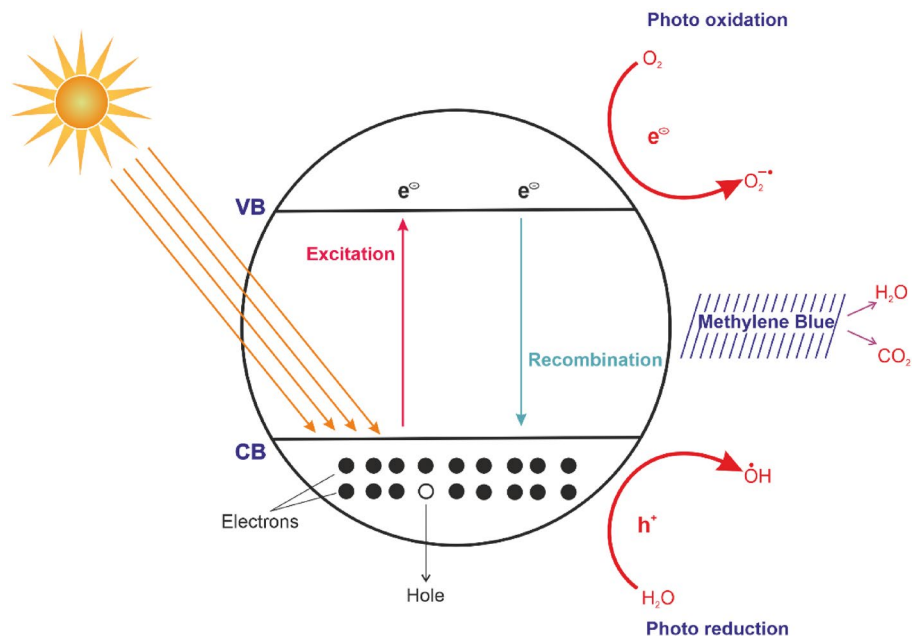**Fig. 14** Schematic illustration of degradation mechanism

Fig. 15 Degradation of MB dye after the irradiation of visible light over $MnWO_4$ nanoparticles during five consecutive photocatalytic cycles

Fig. 16 Photocatalytic activity of the $MnWO_4$ nanoparticles for the degradation of MB dye with different scavengers

4.4 Detection of reactive oxygen species

The impact of reactive species in the breakdown of methylene blue dye was explored using various scavengers, as depicted in Fig. 16. Scavengers, including ethylenediamine tetraacetic acid disodium salt (EDTA-2Na, 1 mM), potassium dichromate ($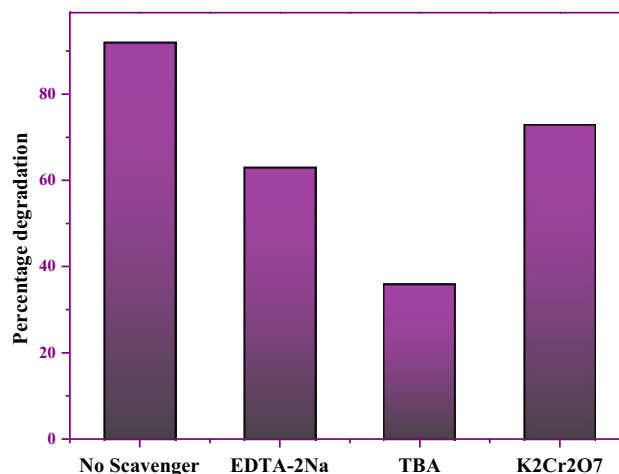K_2Cr_2O_7$, 1 mM), and tert-butyl alcohol (TBA, 1 mM), were employed to scavenge holes (h^+), superoxide anion radical (O^{2-}), and hydroxyl radical ($\bullet OH$), respectively, as illustrated in Fig. 12. The findings showed that the degradation percentage was significantly diminished in the presence of TBA, indicating that hydroxyl radicals play a significant role in the degradation of methylene blue dye. Hydroxyl radicals are a type of reactive oxygen species. As the pH of the solution increases, the number of hydroxide ions also increases. These hydroxides, along with

the water molecules, react with the holes generated at the valence band of the nanoparticles to produce hydroxyl radicals. These hydroxyl radicals are the final and necessary reactive oxygen species required for the degradation of organic compounds. As the number of hydroxides increases, the number of hydroxyl radicals also increases, resulting in the highest oxidative degradation of organic methylene blue. Therefore, at a basic pH, more reactive oxygen species are generated, leading to increased degradation activity.
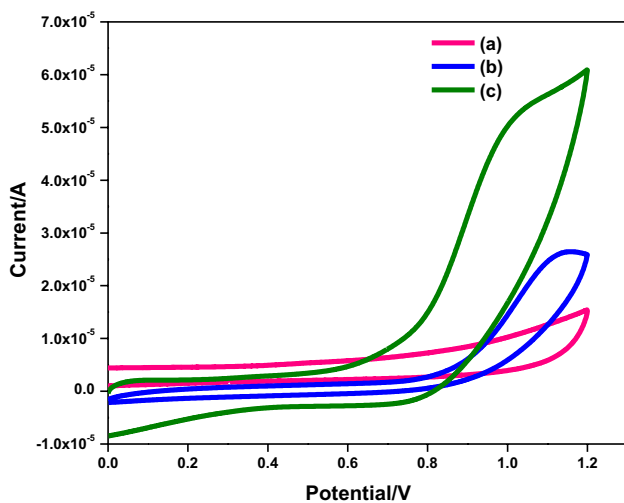

Fig. 17 CV's obtained at **a** bare GCE in the absence of nitrite, **b** bare GCE in presence of 1 mM nitrite **c** MnWO$_4$ modified GCE in presence of 1 mM nitrite

5 Electrochemical sensing of sodium nitrite

To determine the sensing activity of the material MnWO$_4$, it was modified on the surface of a glassy carbon electrode (GCE) and then its cyclic voltammograms were examined in the presence and absence of nitrite along with the bare GCE. A scan rate of 50 mV s^{-1} and a potential window of 1.2 V were utilized. A CV was obtained at a bare GCE in the absence of nitrite, as shown in Fig. 17a, revealing that no oxidation or reduction reactions were occurring at the bare GCE. The CV obtained at the bare GCE in the presence of a 1 mM nitrite solution was shown by curve b in Fig. 17, indicating the oxidation of nitrite at a potential of 1.13 V with a peak current of 26.0 μA. This shows that the bare GCE also has the ability to detect nitrite. The MnWO$_4$ modified GCE (MnWO$_4$/GCE) electrode was then immersed in a solution containing 1 mM nitrite, resulting in the CV shown by curve c in Fig. 17. The peak current was obtained at a voltage of 1.07 V with a peak current of 55.64 μA, which is nearly 2.14 times greater than that of the bare GCE. The oxidation potential of MnWO$_4$ was found to be shifted towards the lower side of the potential window, indicating that the MnWO$_4$/GCE is an efficient electrode as it requires less potential for the oxidation of nitrite. This demonstrates the excellent sensing activity of the MnWO$_4$/GCE for the detection of nitrite at very low concentrations.
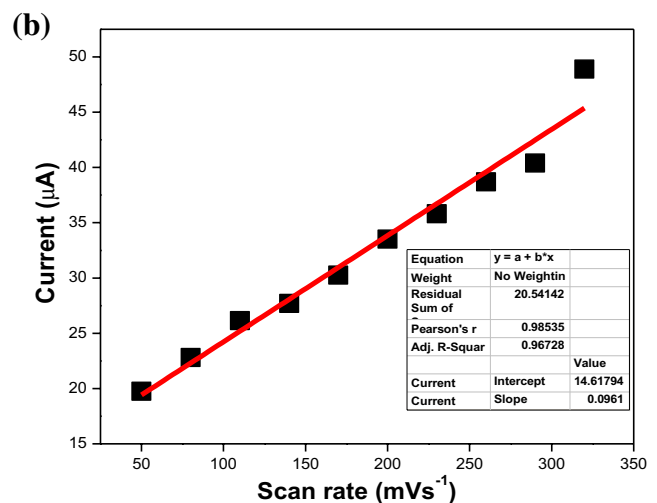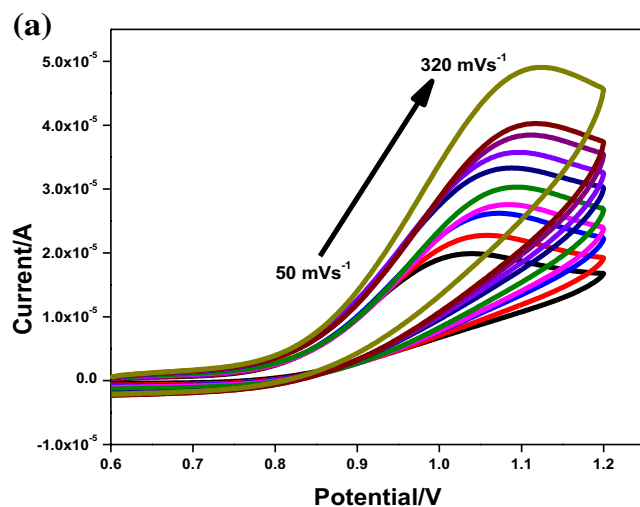

Fig. 18 a CV's obtained at various scan rates using MnWO$_4$ modified GCE in presence of 1 mM nitrite. **b** variation of current vs. scan rates

5.1 Effect of scan rate on nitrite oxidation

The effect of different scan rates on the detection of nitrite was studied to determine the rate of the electrochemical reaction. A constant concentration of nitrite at 0.01 mM was used and $MnWO_4$/GCE was employed as the working electrode. The scan rates were varied from 50 to 320 mVs^{-1} with an interval of 30 mVs^{-1}. The corresponding cyclic voltammograms (CVs) obtained at the varied scan rates are shown in Fig. 18a. The peak currents were found to increase with the scan rates, as shown in Fig. 18b. The peak potentials shifted towards the positive potential as the scan rates increased from 50 to 170 mVs^{-1}, due to the less efficient interaction time of the $MnWO_4$ nanoparticles with nitrite molecules. At higher scan rates, the peak potentials again followed the same trend. A linear regression analysis was conducted, which showed that the relationship between the scan rates and peak currents was evidently linear with a slope of 0.0961 and a correlation coefficient of 0.9853. The linear regression equation was found to be I (μA) = 0.0961 (v) + 14.617 μA. From this, it can be concluded that $MnWO_4$ nanoparticles are efficient electrode materials for the detection of nitrite at a low concentration of 0.01 mM with a low scan rate of 50 mVs^{-1}.

5.2 Electrochemical impedance spectroscopic (EIS) analysis

Electrochemical impedance spectroscopy analysis was performed to assess the electrochemical conductivity of the material $MnWO_4$ by using the modified electrode. The resulting EIS plot is shown in Fig. 19. The obtained data was analyzed using Z-Fit software, and the corresponding equivalent circuit was constructed. The equivalent circuit was found to be R1 + C2/(R2 + W3), where R1 and R2 are resistors, C2 is a capacitance, and W3 is a Warburg element for semi-infinite diffusion. The values for the circuit elements are listed in the table below. This confirms that $MnWO_4$ is an excellent material, with a very low resistance of 147 Ω, and is suitable for all electrochemical applications.

Circuit elements				
Nanomaterial	R_1 (Ω)	R_2 (Ω)	C_2 (F)	W_3 (Ω $s^{-1/2}$)
$MnWO_4$	117.7	32.11	1.577 E^{-9}	-4 601

6 Conclusion

In this study, we have successfully synthesized $MnWO_4$ nanoparticles using a simple thermal decomposition method without the need for any additional fuel for combustion. This approach offers numerous advantages including cost-effectiveness, environmental friendliness, non-toxicity, low temperature requirement, simplicity, and rapidity. The X-ray diffraction (XRD) analysis revealed that the $MnWO_4$ crystals possess a monoclinic structure, with an average crystallite size of 61 nm. The diffuse reflectance spectroscopy (DRS) results indicated a band gap of 2.65 eV for the synthesized $MnWO_4$ nanoparticles. Scanning electron microscopy (SEM) studies demonstrated a uniform distribution of $MnWO_4$
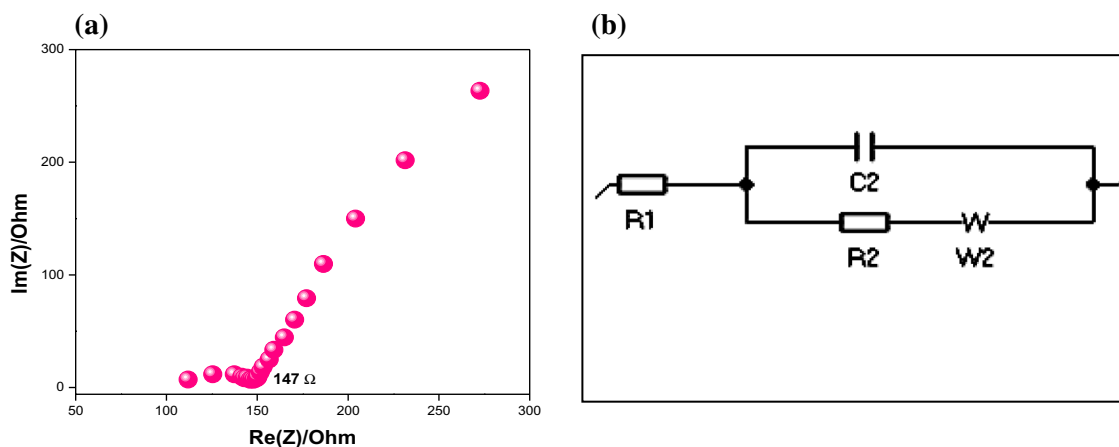

Fig. 19 **a** Electrochemical impedance spectrum of $MnWO_4$. **b** Equivalent circuit obtained for the Impedance plot

particles in terms of shape and size at higher temperatures. The prepared $MnWO_4$ nanoparticles exhibited enhanced stability and excellent photocatalytic activity in the degradation of methylene blue. Additionally, we evaluated the electroanalytical applicability of the synthesized $MnWO_4$ nanostructures by quantifying nitrite at trace concentration levels, demonstrating their potential for various analytical applications.

Acknowledgements

Author contributions

GSS: Data curation, writing—original draft, PP and GN: writing—review and editing. CM: software, validation, LS: investigation, RVL, SP, KCSK: visualization, supervision.

Funding

Data availability

The data that supports the findings of this study are available in the supplementary material of this article.

Declarations

Conflict of interest   Authors do not have any conflict of interest with respect to this paper.

Consent for publication   Not applicable.

References

1. H.N. Deepakumari, V.L. Ranganatha, G. Nagaraju, R. Prakruthi, C. Mallikarjunaswamy, Facile green synthesis of zirconium phosphate nanoparticles using *Aegle marmelos*: antimicrobial and photodegradation studies. Mater. Today Proc. **62**, 5169–5173 (2022)

2. C. Mallikarjunaswamy, P. Parameswara, S. Pramila, G. Nagaraju, H.N. Deepakumari, Green and facile synthesis of zinc oxide nanoparticles for enhanced photocatalytic organic pollutant degradation. J. Mater. Sci. (2022). https://doi.org/10.1007/s10854-022-08852-z

3. V.L. Ranganatha, S. Pramila, G. Nagaraju, B.S. Surendra, C. Mallikarjunaswamy, Cost-effective and green approach for the synthesis of zinc ferrite nanoparticles using *Aegle marmelos* extract as a fuel: catalytic, electrochemical, and microbial applications. J. Mater. Sci. **31**, 1–18 (2020)

4. D.S. Kudlur, A.M. Meghashree, S.A. Vinutha, K.C. Sunil, G. Karthik, P.A. Venkatesh, Materials today: proceedings one pot synthesis of CuO-NiO nanoparticles using *Aegle marmelos* fruit extract and their antimicrobial activity. Mater. Today Proc. (2023). https://doi.org/10.1016/j.matpr.2023.03.256

5. C. Mallikarjunaswamy, J.S. Vidya, H.N. Deepakumari, G. Nagaraju, M.A. Sangamesha, Materials today: proceedings larvicidal and antimicrobial activity of zinc oxide nanoparticles synthesized from rain tree pod aqueous extract. Mater. Today Proc. **62**, 5083–5086 (2022). https://doi.org/10.1016/j.matpr.2022.02.422

6. V.L. Ranganatha, G. Nagaraju, J.S. Vidya, H.N. Deepakumari, D.M. Gurudutt, Materials today: proceedings Indian bael mediated eco-friendly synthesis and performance evaluation of zirconium oxide nanoparticles: an efficient anti-microbial agent. Mater. Today Proc. **62**, 5067–5070 (2022). https://doi.org/10.1016/j.matpr.2022.02.407

7. C. Mallikarjunaswamy, S. Pramila, G. Nagaraju, V. L. Ranganatha, Enhanced photocatalytic, electrochemical and antimicrobial activities of α-$Mn_2V_2O_7$ nanopebbles. J. Mater. Sci. **33**, 617–634 (2022).

8. B.S. Surendra, M.M. Swamy, T. Shamala, S. Rao, A.S. Sowmy, C. Mallikarjuna, S. Pramila, Development of enhanced electrochemical sensor and antimicrobial studies of ZnO NPs synthesized using green plant extract. Sens. Int. **3**, 100176 (2022). https://doi.org/10.1016/j.sintl.2022.100176

9. C.M.V. Lakshmi, R. Ramith, R. Udayabhanu, Facile microwave—assisted green synthesis of ZnO nanoparticles: application to photodegradation, antibacterial and antioxidant. J. Mater. Sci. **31**, 1004–1021 (2020). https://doi.org/10.1007/s10854-019-02612-2

10. D. Malwal, G. Packirisamy, Recent advances in the synthesis of metal oxide (MO) nanostructures. Elsevier Ltd. (2018). https://doi.org/10.1016/B978-0-08-101975-7.00010-5

11. P. Velusamy, R.R. Babu, K. Ramamurthi, E. Elangovan, J. Viegas, Effect of La doping on the structural, optical and electrical properties of spray pyrolytically deposited CdO thin films. J. Alloys Compd. **708**, 804–812 (2017). https://doi.org/10.1016/j.jallcom.2017.03.032

12. C. Mallikarjunaswamy, S. Pramila, G. Nagaraju, R. Ramu, V.L. Ranganatha, Green synthesis and evaluation of antiangiogenic, photocatalytic, and electrochemical activities of $BiVO_4$ nanoparticles. J. Mater. Sci. **32**, 1–19 (2021)

13. P. Velusamy, S. Liu, R. Xing, M. Sathiya, A. Ahmad, M.D. Albaqami, R. Ghazi, E. Elamurugu, M.S. Pandian, P. Ramasamy, ScienceDirect Enhanced photo-electrocatalytic performance of the nano heterostructures based on Pr_3 þ modified. Int. J. Hydrogen Energy **47**, 32903–32920 (2022). https://doi.org/10.1016/j.ijhydene.2022.07.177

14. P. Velusamy, X. Liu, M. Sathiya, N.S. Alsaiari, F.M. Alzahrani, M.T. Nazir, E. Elamurugu, M.S. Pandian, F. Zhang, Investigate the suitability of g-C3N4 nanosheets ornamented with BiOI nanoflowers for photocatalytic dye degradation and PEC water splitting. Chemosphere **321**, 138007 (2023)

15. C. Mallikarjunaswamy, S. Pramila, G.S. Shivaganga, H.N. Deepakumari, R. Prakruthi, G. Nagaraju, P. Parameswara, V. L. Ranganatha. Facile synthesis of multifunctional bismuth oxychloride nanoparticles for photocatalysis and antimicrobial test. Mater. Sci. Eng. B 290, 116323 (2023). https://doi.org/10.1016/j.mseb.2023.116323.

16. V.A. Online, R. Ramesh, RSC Adv. (2015). https://doi.org/10.1039/C5RA15262C

17. H.N. Cuong, S. Pansambal, S. Ghotekar, R. Oza, N.T.T. Hai, N.M. Viet, V.-H. Nguyen, New frontiers in the plant extract mediated biosynthesis of copper oxide (CuO) nanoparticles and their potential applications: a review. Environ. Res. **203**, 111858 (2022)

18. S. Pramila, V.L. Ranganatha, G. Nagaraju, C. Mallikarjunaswamy, Microwave and combustion methods: a comparative study of synthesis, characterization, and applications of NiO nanoparticles. Inorg. Nano-Metal Chem. (2022). https://doi.org/10.1080/24701556.2022.2081188

19. S. Pramila, V.L. Ranganatha, G. Nagaraju, C. Mallikarjunaswamy, Green synthesis of bismuth tungstate nanoparticles, evaluation of their applications favouring photocatalytic and bio-sensing. Inorg. Nano-Metal Chem. (2022). https://doi.org/10.1080/24701556.2022.2081192

20. M. Aravind, M. Amalanathan, S. Aslam, A.E. Noor, D. Jini, S. Majeed, P. Velusamy, A.A. Alothman, R.A. Alshgari, M.S.S. Mushab, Hydrothermally synthesized Ag-TiO_2 nanofibers (NFs) for photocatalytic dye degradation and antibacterial activity. Chemosphere **321**, 138077 (2023)

21. S.A. Vinutha, A.M. Meghashree, D.M. Gurudutt, D.S. Kudlur, K.C.S. Kumar, G. Karthik, N.A. Kumar, V.L. Ranganatha, P. Parameswara, C. Mallikarjunaswamy, Materials today: proceedings Facile green synthesis of cerium oxide nanoparticles using Jacaranda mimosifolia leaf extract and evaluation of their antibacterial and photodegradation activity. Mater. Today Proc. (2023). https://doi.org/10.1016/j.matpr.2023.05.592

22. R. Krishnan, S. N. Shibu, D. Poelman, A. K. Badyal, A. Kunti, H. C. Swart, S. G. Menon, Recent advances in microwave synthesis for photoluminescence and photocatalysis. Mater. Today Commun. **32**, 103890 (2022).

23. D.D. Mal, D. Pradhan, Room temperature acid-free greener synthesis of imine using cobalt-doped manganese tungstate. Inorg. Chem. **61**, 2211–2218 (2022)

24. H. Eranjaneya, G.T. Chandrappa, Solution combustion synthesis of nano $ZnWO_4$ photocatalyst. Trans. Indian Ceram. Soc. **75**, 133–137 (2016)

25. Q. Zou, R. Tang, H. Zhao, J. Jiang, J. Li, Y. Fu, Hyaluronic-acid-assisted facile synthesis of $MnWO_4$ single-nanoparticle for efficient trimodal imaging and liver–renal structure display. ACS Appl. Nano Mater. **1**, 101–110 (2017)

26. M. Rahimi-Nasrabadi, M. Eghbali-Arani, The effect of sugars on the morphology of $MnWO_4$ nanoparticles, and evaluating the product as photocatalysts. J. Mater. Sci. **28**, 15239–15245 (2017)

27. F. Li, X. Xu, J. Huo, W. Wang, A simple synthesis of $MnWO_4$ nanoparticles as a novel energy storage material. Mater. Chem. Phys. **167**, 22–27 (2015)

28. H. Zhou, J. Ke, H. Wu, J. Liu, D. Xu, X. Zou, Manganese tungstate/graphitic carbon nitride S-scheme heterojunction for boosting hydrogen evolution and mechanism exploration. Mater. Today Energy **23**, 100918 (2022)

29. L.H. Hoang, N.T.M. Hien, W.S. Choi, Y.S. Lee, K. Taniguchi, T. Arima, S. Yoon, X.B. Chen, I. Yang, Temperature-dependent Raman scattering study of multiferroic $MnWO_4$. J Raman Sepectrosc **4**(2009), 1005–1010 (2010). https://doi.org/10.1002/jrs.2542

30. Y. Wang, L. Yang, Y. Wang, X. Wang, G. Han, Shape-controlled synthesis of $MnWO_4$ nanocrystals by a surfactant-free hydrothermal method. Ceram. Int. **40**, 5085–5090 (2014). https://doi.org/10.1016/j.ceramint.2013.09.117

31. G. Harichandran, P. Divya, S. Radha, J. Yesuraj, Facile and controllable CTAB-assisted sonochemical synthesis of one-dimensional $MnWO_4$ nanorods for supercapacitor application. J. Mol. Struct. **1199**, 126931 (2020). https://doi.org/10.1016/j.molstruc.2019.126931

32. M. Khaksar, D.M. Boghaei, M. Amini, Synthesis, structural characterization and reactivity of manganese tungstate nanoparticles in the oxidative degradation of methylene blue. C. R.

Chim. **18**, 199–203 (2015). https://doi.org/10.1016/j.crci.2014.04.004

33. P. Van Hanh, L. H. Hoang, P. Van Hai, N. Van Minh, X.B. Chen, I.S. Yang, Crystal quality and optical property of $MnWO_4$ nanoparticles synthesized by microwave-assisted method. J. Phys. Chem. Solids. **74**, 426–430 (2013)

34. L. Yang, Y. Wang, Y. Wang, X. Wang, L. Wang, G. Han, Shape-controlled synthesis of $MnWO_4$ nanocrystals via a simple hydrothermal method. J. Alloys Compd. **578**, 215–219 (2013). https://doi.org/10.1016/j.jallcom.2013.05.133

35. H. Eranjaneya, P.S. Adarakatti, A. Siddaramanna, P. Malingappa, G.T. Chandrappa, Citric acid assisted synthesis of manganese tungstate nanoparticles for simultaneous electrochemical sensing of heavy metal ions. Mater. Sci. Semicond. Process. **86**, 85–92 (2018). https://doi.org/10.1016/j.mssp.2018.06.020

36. W.B. Hu, X.L. Nie, Y.Z. Mi, Controlled synthesis and structure characterization of nanostructured $MnWO_4$. Mater. Charact. **61**, 85–89 (2010). https://doi.org/10.1016/j.matchar.2009.10.009

37. W. Qu, W. Wlodarski, J.U. Meyer, Comparative study on micromorphology and humidity sensitive properties of thin-film and thick-film humidity sensors based on semiconducting $MnWO_4$. Sens. Actuators B **64**, 76–82 (2000). https://doi.org/10.1016/S0925-4005(99)00487-6

38. M. Rahimi-Nasrabadi, S.M. Pourmortazavi, M. Khalilian-Shalamzari, S.S. Hajimirsadeghi, M.M. Zahedi, Optimization of synthesis procedure and structure characterization of manganese tungstate nanoplates. Cent. Eur. J. Chem. **11**, 1393–1401 (2013). https://doi.org/10.2478/s11532-013-0271-y

39. S. Zinatloo-Ajabshir, M. Baladi, M. Salavati-Niasari, Sono-synthesis of $MnWO_4$ ceramic nanomaterials as highly efficient photocatalysts for the decomposition of toxic pollutants. Ceram. Int. **47**, 30178–30187 (2021). https://doi.org/10.1016/j.ceramint.2021.07.197

40. S. Saranya, R.K. Selvan, N. Priyadharsini, Synthesis and characterization of polyaniline/$MnWO_4$ nanocomposites as electrodes for pseudocapacitors. Appl. Surf. Sci. **258**, 4881–4887 (2012). https://doi.org/10.1016/j.apsusc.2012.01.104

41. S. Saranya, S.T. Senthilkumar, K.V. Sankar, R.K. Selvan, Synthesis of $MnWO_4$ nanorods and its electrical and electrochemical properties. J. Electroceram. **28**, 220–225 (2012). https://doi.org/10.1007/s10832-012-9714-7

42. S. Muthamizh, R. Suresh, K. Giribabu, R. Manigandan, S.P. Kumar, S. Munusamy, V. Narayanan, $MnWO_4$ nanocapsules: synthesis, characterization and its electrochemical sensing property. J. Alloys Compd. **619**, 601–609 (2015). https://doi.org/10.1016/j.jallcom.2014.09.049

43. C.P. Devatha, A.K. Thalla, Green synthesis of nanomaterials. In: Synthesis of Inorganic Nanomaterials (pp. 169–184). Elsevier, New York (2018).

44. G. Karkera, T. Sarkar, M.D. Bharadwaj, A.S. Prakash, Design and development of efficient bifunctional catalysts by tuning the electronic properties of cobalt–manganese tungstate for oxygen reduction and evolution reactions. ChemCatChem **9**, 3681–3690 (2017)

45. N.D. Cuong, K.Q. Trung, T.-D. Nguyen, N. Van Toan, C.M. Hung, N. Van Hieu, Controlled synthesis of manganese tungstate nanorods for highly selective NH_3 gas sensor. J. Alloys Compd. **735**, 787–794 (2018)

46. T.L. Soundarya, R. Harini, K. Manjunath, ScienceDirect Pt-doped TiO_2 nanotubes as photocatalysts and electrocatalysts for enhanced photocatalytic H_2 generation, electrochemical sensing, and supercapacitor applications. Int. J. Hydrogen Energy. (2023). https://doi.org/10.1016/j.ijhydene.2023.04.289

47. T.L. Soundarya, B. Nirmala, F.A. Alharthi, B. Nagaraj, G. Nagaraju, HRSL supported fabrication of $LiZnVO_4$ nanoparticles: applications to photoluminescence, dye elimination and biosensing Materials Science & Engineering B HRSL supported fabrication of $LiZnVO_4$ nanoparticles: applications to photoluminescence, dye Elim. Mater. Sci. Eng. B **280**, 115718 (2022). https://doi.org/10.1016/j.mseb.2022.115718

48. T.L. Soundarya, Y.T. Ravikiran, B. Nirmala, G. Nagaraju, Green synthesis of $LiZnVO_4$ nanoparticles and its multiple applications towards electrochemical sensor, supercapacitor, humidity sensing, photoluminescence and antioxidant activities. J. Mater. Sci. (2022). https://doi.org/10.1007/s10854-022-08070-7

49. X. Lin, J. Xing, W. Wang, Z. Shan, F. Xu, F. Huang, Photocatalytic activities of heterojunction semiconductors Bi_2O_3/$BaTiO_3$: a strategy for the design of efficient combined photocatalysts. J. Phys. Chem. C **111**, 18288–18293 (2007)

50. P. Van Hanh, L.H. Hoang, P. Van Hai, N. Van Minh, X.-B. Chen, I.-S. Yang, Crystal quality and optical property of $MnWO_4$ nanoparticles synthesized by microwave-assisted method. J. Phys. Chem. Solids. **74**, 426–430 (2013)